Table 1. Performance summary for the three algorithm variants. Baseline algorithms 1 and 2 disable the iterative and the model-driven nature of the learning process, respectively, while ensuring that the same computational effort and number of physical actions are used. Before damage, a successful experiment is determined as one that outputs a model with correct topology (see fig. S2 for examples of correct and incorrect topologies). Mean model error was calculated over the best model from each of the 30 experiments. Mean values are reported ± SD. An additional 90 experiments were conducted after the robot was damaged. The robot reinitiates modeling at this point using the most accurate model from the first 90 experiments (Fig. 2F). In this case, mean model error is determined as the difference between the inferred length of the damaged leg and the true damaged length (9.7 cm).

	Baseline 1	Baseline 2	Model-driven algorithm
Before damage			
Independent experiments (n)	30	30	30
Physical actions per experiment	16	16	16
Mean model evaluations ($n = 30$)	262,080 ± 13,859	246,893 ± 17,469	262,024 ± 13,851
Successful self-models	7	8	13
Success rate	23.3%	26.7%	43.3%
Mean model error ($n = 30$)	9.62 ± 1.47 cm	9.7 ± 1.45 cm	7.31 ± 1.22 cm
After damage			
Independent experiments (n)	30	30	30
Physical actions per experiment	16	16	16
Mean model evaluations ($n = 30$)	292,430 ± 44,375	278,140 ± 37,576	296,000 ± 22,351
Mean model error ($n = 30$)	5.60 ± 2.98 cm	4.55 ± 3.22 cm	2.17 ± 0.55 cm

Fig. 3. Distance traveled during optimized versus random behaviors. Dots indicate the final location of the robot's center of mass, when it starts at the origin. Red dots indicate final positions of the physical robot when executing random behaviors. Black dots indicate final expected positions predicted by the 30 optimized behaviors when executed on the self-model (Fig. 2F). Blue dots denote the actual final positions of the physical robot after executing those same behaviors in reality. The behaviors corresponding to the circled dots are depicted in Fig. 2, G to L. Squares indicate mean final positions. Vertical and horizontal lines indicate 2 SD for vertical and horizontal displacements, respectively.

not fast enough to provide adequate feedback during rapid and complex motion (*29*). Although it is unlikely that organisms maintain explicit models such as those presented here, the proposed method may shed light on the unknown processes by which organisms actively create and update self-models in the brain, how and which sensor-motor signals are used to do this, what form these models take, and the utility of multiple competing models (*30*). In particular, this work suggests that directed exploration for acquisition of predictive self-models (*31*) may play a critical role in achieving higher levels of machine cognition.

References and Notes
1. B. Webb, *Behav. Brain Sci.* **24**, 1033 (2001).
2. R. Arkin, *Behavior-Based Robotics* (MIT Press, Cambridge, MA, 1998).
3. R. J. Full, D. E. Koditschek, *J. Exp. Biol.* **202**, 3325 (1999).
4. R. Pfeifer, *Int. J. Cognit. Technol.* **1**, 125 (2002).
5. T. Christaller, *Artif. Life Robot.* **3**, 221 (1999).
6. S. Nolfi, D. Floreano, *Evolutionary Robotics: The Biology, Intelligence, and Technology of Self-Organizing Machines* (MIT Press, Cambridge, MA, 2000).
7. S. H. Collins, A. Ruina, R. Tedrake, M. Wisse, *Science* **307**, 1082 (2005).
8. S. Thrun, W. Burgard, D. Fox, *Probabilistic Robotics* (MIT Press, Cambridge, MA, 2005).
9. L. Sciavicco, B. Siciliano, *Modelling and Control of Robot Manipulators* (Springer-Verlag, London, 2001).
10. E. Alpaydin, *Introduction to Machine Learning* (MIT Press, Cambridge, MA, 2004).
11. K. Kozlowski, *Modelling and Identification in Robotics* (Springer-Verlag, London, 1998).
12. L. Ljung, *System Identification: Theory for the User* (Prentice-Hall, Englewood Cliffs, NJ, 1999).
13. D. Keymeulen, M. Iwata, Y. Kuniyoshi, T. Higuchi, *Artif. Life* **4**, 359 (1998).
14. P. F. M. J. Verschure, T. Voegtlin, R. J. Douglas, *Nature* **425**, 620 (2003).
15. G. S. Hornby, S. Takamura, T. Yamamoto, M. Fujita, *IEEE Trans. Robot.* **21**, 402 (2005).
16. R. Pfeifer, C. Scheier, *Understanding Intelligence* (MIT Press, Cambridge, MA, 1999).
17. S. H. Mahdavi, P. Bentley, *Auton. Robots* **20**, 149 (2006).
18. M. L. Visinsky, J. R. Cavallaro, I. D. Walker, *Reliab. Eng. Syst. Saf.* **46**, 139 (1994).
19. F. Caccavale, L. Villani, P. Ax, Eds., *Fault Diagnosis and Fault Tolerance for Mechatronic Systems* (Springer Verlag, New York, 2002).
20. S. Zilberstein, R. Washington, D. S. Benstein, A.-I. Mouaddib, *Lect. Notes Comput. Sci.* **2466**, 270 (2002).
21. H. S. Seung, M. Opper, H. Sompolinsky, in *Proceedings of the 5th Workshop on Computational Learning Theory* (ACM Press, New York, 1992), pp. 287–294.
22. J. Bongard, H. Lipson, *J. Mach. Learn. Res.* **6**, 1651 (2005).
23. J. Bongard, H. Lipson, *Trans. Evol. Comput.* **9**, 361 (2005).
24. B. Kouchmeshky, W. Aquino, J. Bongard, H. Lipson, *Int. J. Numer. Methods Eng.*, in press; published online 31 July 2006 (doi: 10.1002/nme.1803).
25. Materials and methods are available as supporting material on *Science* Online.
26. R. A. Brooks, in *Proceedings of the 1st European Conference on Artificial Life,* F. J. Varela, P. Bourgine, Eds. (Springer-Verlag, Berlin, 1992), pp. 3–10.
27. R. D. King *et al.*, *Nature* **427**, 247 (2004).
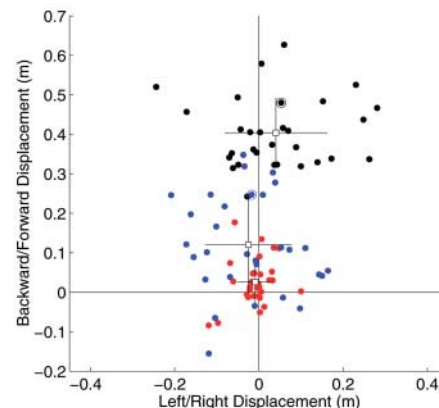28. U. Saranli, M. Buehler, D. E. Koditschek, *Int. J. Robot. Res.* **20**, 616 (2001).
29. A. Maravita, C. Spence, J. Driver, *Curr. Biol.* **13**, R531 (2003).
30. G. Edelman, *Neural Darwinism: The Theory of Neuronal Group Selection* (Basic Books, New York, 1987).
31. F. Crick, C. Koch, *Nat. Neurosci.* **6**, 119 (2003).
32. This research was supported in part by the NASA Program for Research in Intelligent Systems under grant NNA04CL10A and the NSF grant number DMI 0547376.

Solid-State Thermal Rectifier

C. W. Chang,[1,4] D. Okawa,[1] A. Majumdar,[2,3,4] A. Zettl[1,3,4]*

We demonstrated nanoscale solid-state thermal rectification. High-thermal-conductivity carbon and boron nitride nanotubes were mass-loaded externally and inhomogeneously with heavy molecules. The resulting nanoscale system yields asymmetric axial thermal conductance with greater heat flow in the direction of decreasing mass density. The effect cannot be explained by ordinary perturbative wave theories, and instead we suggest that solitons may be responsible for the phenomenon. Considering the important role of electrical rectifiers (diodes) in electronics, thermal rectifiers have substantial implications for diverse thermal management problems, ranging from nanoscale calorimeters to microelectronic processors to macroscopic refrigerators and energy-saving buildings.

The invention of nonlinear solid-state devices, such as diodes and transistors, that control electrical conduction marked the emergence of modern electronics. It is apparent that counterpart devices for heat conduction, if they could be fabricated, would have

deep implications for thermal circuits, thermal management, and the field of phononics in general. In recent years, some theoretical proposals for thermal rectifiers have been put forward (1–4), but these usually require complex coupling between individual atoms and substrates that are difficult to achieve experimentally. However, as noted by Peierls (5), heat transport in one dimension can be anomalous, and the breakdown of Fourier's law in one-dimensional (1D) systems may be coupled with extraordinary nonlinear thermal effects (6), including rectification.

Nanotubes are nearly 1D and thus are ideal materials for exploring thermal rectification effects. Previous studies have demonstrated that the thermal conductivity of 1D carbon nanotubes (CNTs) and boron nitride nanotubes (BNNTs) is high and dominated by phonons (7, 8). For unmodified nanotubes with uniform mass distribution, the thermal conductance is symmetric (i.e., independent of the direction of axial heat flow). To investigate asymmetric thermal propagation in a suitable 1D inhomogeneous medium, we modified CNTs and BNNTs so that they assumed a non-uniform axial mass distribution (Fig. 1).

Pristine multiwalled BNNTs were first synthesized by means of an adaptation of a previously reported method (9), yielding samples with a typical outer diameter of ~30 to 40 nm and a length of ~10 μm. High-quality CNTs with diameters ranging from 10 to 33 nm were prepared by means of conventional arc methods (10). Individual tubes were placed on a custom-designed microscale thermal conductivity test fixture (11), with the use of a piezo-driven manipulator operated inside a scanning electron microscope (SEM). In brief, the fixture incorporates independently suspended SiN_x pads, with symmetrically fabricated Pt film resistors serving as either heaters or sensors. One end of the nanotube was bonded to the heater, the other end was bonded to the sensor, and the body of the nanotube was suspended in the vacuum in between.

Figure 2A shows an SEM image of a multiwalled CNT mounted to the test fixture and B the corresponding low-magnification transmission electron microscopic (TEM) image of the same CNT. For thermal conductance measurements, a known power P was supplied to the heater while resistance changes of the heater and sensor were used to determine the resulting temperature changes of the heater

¹Department of Physics, University of California at Berkeley, Berkeley, CA 94720, USA. ²Departments of Mechanical Engineering and Materials Science and Engineering, University of California at Berkeley, Berkeley, CA 94720, USA. ³Materials Sciences Division, Lawrence Berkeley National Laboratory, Berkeley, CA 94720, USA. ⁴Center of Integrated Nanomechanical Systems, University of California at Berkeley, Berkeley, CA 94720, USA.

*To whom correspondence should be addressed. E-mail: azettl@berkeley.edu

(ΔT_h) and sensor (ΔT_s) pads. The thermal conductance K of the nanotube was determined from ΔT_h and ΔT_s with the use of the relation

$$K = \frac{P}{\Delta T_h - \Delta T_s}\left(\frac{\Delta T_s}{\Delta T_h + \Delta T_s}\right) \quad (1)$$

Because of unavoidable non-uniformities in the construction of the test fixture itself, the system with the attached pristine nanotube was first calibrated to establish residual asymmetry by switching the roles of the heater and sensor. All the measurements were done at room temperature.

Nanotubes were engineered in situ while mounted to the test fixture in the SEM. Trimethyl-cyclopentadienyl platinum ($C_9H_{16}Pt$) was deposited non-uniformly along the length of the nanotube in an attempt to achieve the non-uniform mass-loading geometry depicted in Fig. 1. Figure 2C shows a TEM image of the same CNT as in Fig. 2, A and B, after mass loading. The deposited $C_9H_{16}Pt$ was found to be amorphous and tightly bound to the CNT. The sample mass near the right contact has clearly been increased (Fig. 2C). Indeed, the mass loading is even more effective than Fig. 2C might

suggest: The molecular weight of $C_9H_{16}Pt$ (~319 g/mol) is much larger than that of $(C–C)_5$ or $(BN)_5$ (~120 g/mol), and because the molecular volumes are similar, the mass density is correspondingly higher as well.

Depositing $C_9H_{16}Pt$ on a nanotube has several possible effects on the sample thermal conductance. The most obvious is that the fused $C_9H_{16}Pt$ forms an additional thermal conductance channel on parts of the sample. To test for the magnitude of this symmetrical enhancement, we suspended the fused $C_9H_{16}Pt$ across the test fixture pads and measured its thermal conductance. At room temperature, the thermal conductivity of $C_9H_{16}Pt$ was found to be temperature-independent and less than 1% of that of the nanotube. Hence, its direct thermal contribution can be neglected.

After mass loading, the thermal conductance of the nanotube was again tested in both directions. Thermal rectification of the nanotube is defined as

$$Rectification = \frac{K_{H \to L} - K_{L \to H}}{K_{L \to H}} \times 100\% \quad (2)$$

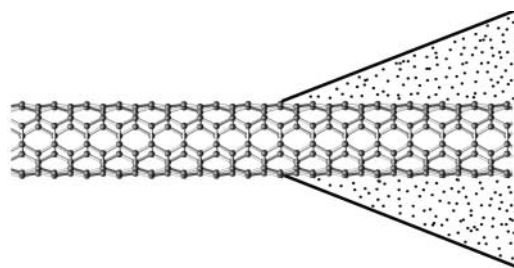**Fig. 1.** A schematic description of depositing amorphous $C_9H_{16}Pt$ (black dots) on a nanotube (lattice structure).
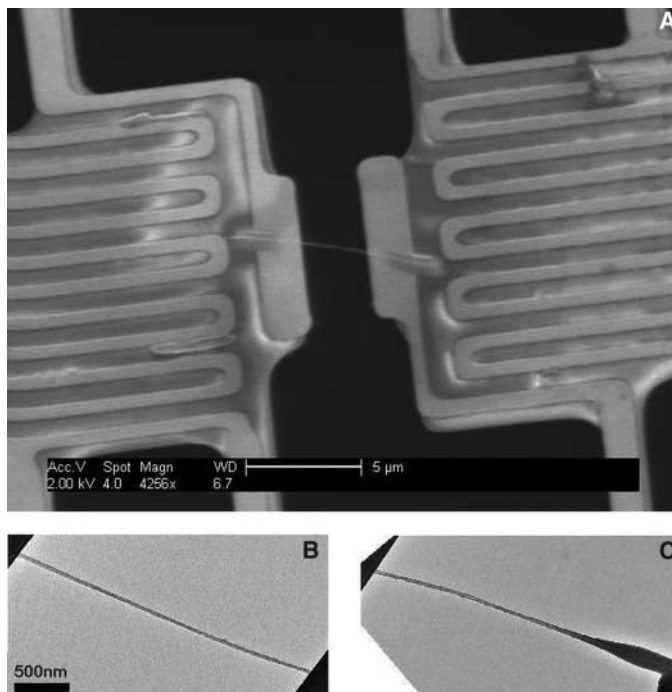

Fig. 2. (**A**) The SEM image of a CNT (light gray line in center) connected to the electrodes. Scale bar, 5 μm. (**B** and **C**) The corresponding low-magnification TEM images of the same CNT in (A), before (B) and after (C) $C_9H_{16}Pt$ was deposited.

where $K_{L \to H}$ and $K_{H \to L}$ are the thermal conductances of the nanotube when heat flows from low-mass to high-mass ends or from high-mass to low-mass ends, respectively. For the CNT in Fig. 2, the measured thermal conductivity was 305 W/(m·K), and the rectification effect at room temperature was 2%.

Figure 3, A to C, shows three BNNTs that were also mass-engineered with $C_9H_{16}Pt$. The respective thermal rectifications were found to be 7, 4, and 3%. The arrows in Fig. 3 denote the direction of heat flow in which a higher thermal conductance was observed. All measurements showed that a higher thermal conductance was observed when heat flowed from the high-mass region (where more $C_9H_{16}Pt$ was deposited) to the low-mass region. Because electrons do not contribute to the thermal transport for BNNTs, the observed rectification effects can be attributed to nonelectronic excitations.

Figure 3D shows, in detail, the relation of ΔT_h versus ΔT_s for the BNNT of Fig. 3A before and after the deposition of $C_9H_{16}Pt$. Equation 1 can be expressed as $Ps/\Delta T_h(1 - s^2)$, which, for $s \equiv \Delta T_s/\Delta T_h \ll 1$, reduces to $Ps/\Delta T_h$. Thus, the slope of the ΔT_h versus ΔT_s curve is proportional to absolute thermal conductance. $K_{L \to H}$ and $K_{H \to L}$ of the pristine nanotube are symmetric. After mass loading, $K_{H \to L}$ and $K_{L \to H}$ differ by 7%, well above the measurement uncertainty (~1%).

We now examine the origin of the observed thermal rectification. An asymmetric geometrical shape can, in principle, introduce asymmetric boundary scattering of phonons, whereby the thermal conductance can be reduced in one direction while it is increased in the other direction. In this scenario, thermal conductance is higher when heat flows from

the narrow region to a wide region. Using the definition of Eq. 2, this always leads to a negative rectification coefficient, even for models where the boundary-scattering coefficient is mass-dependent. However, the thermal rectification observed in our experiments was always positive, and therefore any effect due to asymmetric shape was not dominant. Indeed, the sp^2 bonds in nanotubes are qualitatively much stronger than the bonds between fused $C_9H_{16}Pt$ molecules; thus, phonons should be mainly confined within the nanotubes, with relatively minor geometrical boundary-scattering effects.

A worthwhile analogy can also be made to photon wave propagation. The reflectivity R and the reflection coefficient r of a wave propagating across different media follow

$$R = r^2 = \left(\frac{k_i - k_t}{k_i + k_t} \right)^2 \qquad (3)$$

where k_i and k_t are the wave numbers of incident waves and transmitted waves, respectively. The squaring of the expression in Eq. 3 ensures that R is independent of the direction of incident waves. Because phonons are quanta of waves, the above result demonstrates that thermal rectification is not expected for ordinary wave transport. Similarly, impedance mismatching due to contact resistance will not lead to thermal rectification. In addition, nonlinear perturbative effects such as umklapp processes only decrease the total thermal conductance of the nanotube, without rectification.

Theoretical work has suggested the presence of stable solitons in nanotubes (12, 13). Solitons are nonperturbative solutions of non-

linear systems. They are localized particle-like entities that can collide with each other without changing shape. Within a general class of soliton models, asymmetry of heat flow for an inhomogeneous medium is a common feature (14–16). As an example, the reflection amplitude r for the Korteweg–de Veries equation is (14)

$$r = \begin{cases} 0 & \left(v = \sqrt{\tfrac{m_2}{m_1}} \leq 1 \right) \text{no soliton} \\ \left(\sqrt{2\tfrac{v-1}{v+1} + \tfrac{1}{4}} - \tfrac{1}{2} \right)^2 & \left(v = \sqrt{\tfrac{m_2}{m_1}} > 1 \right) \text{one soliton} \end{cases}$$

$$(4)$$

where m_1 and m_2 are the mass of atoms whose displacement constitutes the incident and transmitted waves, respectively. The most important result of Eq. 4 is the asymmetry with respect to m_2/m_1. The direction of the thermal rectification is positive (better heat flow from high- to low-mass regions), which is consistent with the engineered nanotube rectification results presented above. For a crude estimate of the magnitude of the rectification effect, Eq. 4 yields a rectification of ~7% for a m_2/m_1 of ~5 [close to the molecular weight ratio of $C_9H_{16}Pt$ to $(C–C)_5$ or $(BN)_5$], consistent with the 2 to 7% rectification effects observed for mass-loaded nanotubes. Obviously, more-refined models of soliton transport in mass-loaded nanotubes, taking into account details of geometry, elastic constants, and mass distributions, are needed; but the key point is that linear or nonlinear perturbative systems do not lead to thermal rectification, whereas nonperturbative soliton models naturally do. The stronger ionic nature of BNNTs over CNTs also favors the non-linearity. This may be the reason why BNNTs show a larger thermal rectification effect than CNTs.

With the availability of nonlinear thermal control, phonons should no longer be considered the unwanted by-products of electronics. Phonons, like electrons and photons, are information carriers and should be processed accordingly. Historically, semiconductor- or superconductor-based devices have been used to access thermal signals as soon as they are generated. Thermal rectifiers should make it possible to process thermal currents independently and convert them into electronic signals only when it is most efficient to do so.

Fig. 3. (A to C) SEM images of three different BNNTs after deposition of $C_9H_{16}Pt$. The rectification measured was 7, 4, and 3%. The arrows denote the direction of heat flow, indicating where the thermal conductance is higher than that of the opposite direction. (D) Graphical representation of ΔT_h and ΔT_s for the BNNT in (A) before and after deposition of $C_9H_{16}Pt$. The solid lines are best-fit slopes intersecting the origin. For clarity, only data collected over a limited range of ΔT_h and ΔT_s are shown; data of similar quality were obtained over a much wider range of ΔT_h and ΔT_s.

References and Notes
1. G. Casati, *Chaos* **15**, 015120 (2005).
2. B. W. Li, L. Wang, G. Casati, *Phys. Rev. Lett.* **93**, 184301 (2004).
3. D. Segal, A. Nitzan, *Phys. Rev. Lett.* **94**, 034301 (2005).
4. M. Terraneo, M. Peyrard, G. Casati, *Phys. Rev. Lett.* **88**, 094302 (2002).
5. R. E. Peierls, *Quantum Theory of Solids* (Oxford Univ. Press, London, 1955).
6. For a review, see S. Lepri, R. Livi, A. Politi, *Phys. Rep.* **377**, 1 (2003).
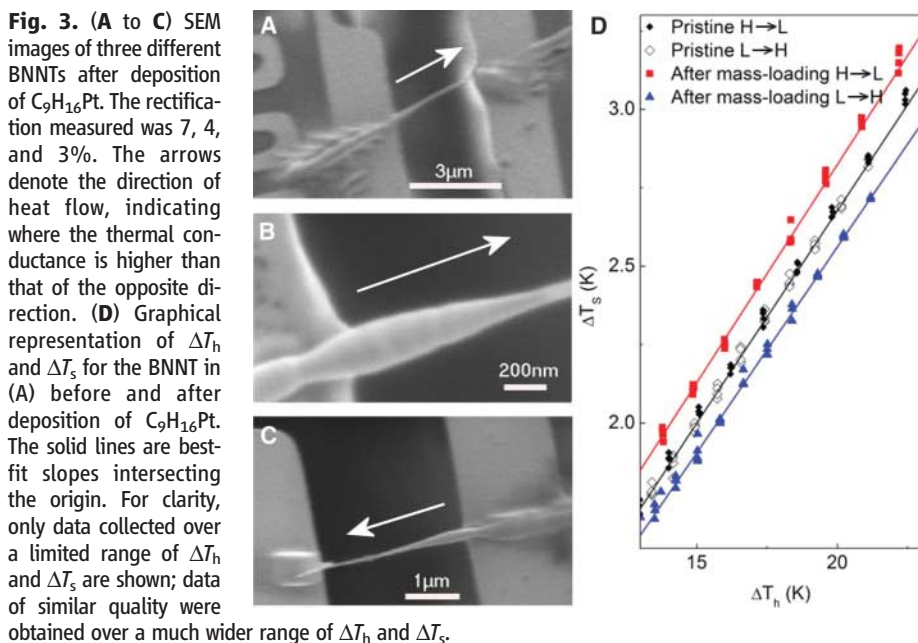
7. C. W. Chang, W. Q. Han, A. Zettl, *J. Vac. Sci. Technol. B* **23**, 1883 (2005).
8. J. Hone, M. Whitney, C. Piskoti, A. Zettl, *Phys. Rev. B* **59**, R2514 (1999).
9. C. Tang, Y. Bando, T. Sato, K. Kurashima, *Chem. Commun.* 1290 (2002).
10. D. T. Colbert *et al.*, *Science* **266**, 1218 (1994).
11. L. Shi *et al.*, *J. Heat Transfer* **125**, 881 (2003).

12. T. Y. Astakhova, O. D. Gurin, M. Menon, G. A. Vinogradov, *Phys. Rev. B* **64**, 035418 (2001).
13. A. V. Savin, O. I. Savina, *Phys. Solid State* **46**, 383 (2004).
14. T. Iizuka, M. Wadati, *J. Phys. Soc. Jpn.* **61**, 3077 (1992).
15. S. Sakai, M. R. Samuelsen, O. H. Olsen, *Phys. Rev. B* **36**, 217 (1987).

16. P. Woafo, *Phys. Rev. E* **58**, 1033 (1998).
17. This work was supported in part by the U.S. Department of Energy and by NSF within the Center of Integrated Nanomechanical Systems.

Reversible, Metal-Free Hydrogen Activation

Gregory C. Welch, Ronan R. San Juan, Jason D. Masuda, Douglas W. Stephan*

Although reversible covalent activation of molecular hydrogen (H₂) is a common reaction at transition metal centers, it has proven elusive in compounds of the lighter elements. We report that the compound $(C_6H_2Me_3)_2PH(C_6F_4)BH(C_6F_5)_2$ (Me, methyl), which we derived through an unusual reaction involving dimesitylphosphine substitution at a para carbon of tris(pentafluorophenyl) borane, cleanly loses H₂ at temperatures above 100°C. Preliminary kinetic studies reveal this process to be first order. Remarkably, the dehydrogenated product $(C_6H_2Me_3)_2P(C_6F_4)B(C_6F_5)_2$ is stable and reacts with 1 atmosphere of H₂ at 25°C to reform the starting complex. Deuteration studies were also carried out to probe the mechanism.

The generation and use of H₂ are important processes to fundamental chemical transformations (*1–7*) and biological functions (*8*). The overwhelming majority of systems known to either liberate or react with H₂ involve reaction at a transition metal center. Hydrogenase enzymes, as well as a plethora of synthetic stoichiometric and catalytic reagents for hydrogenation reactions, are based on the processes of oxidative addition and reductive elimination of H₂ at a metal center. Metal-free systems that either react with or liberate H₂ are rare. A unique metal-free hydrogenase from methanogenic archaea has been shown to catalyze reactions with H₂ (*9–11*), and theoretical studies suggest the role of a folate-like cofactor in the reversible activation or liberation of H₂ (*12, 13*). Several metal-free systems have been shown to activate H₂. For example, main group element–H₂ reactions (*14*) in low-temperature matrices have been reported (*15–17*), and computational studies have probed the occurrence of H₂ bonds in main-group compounds (*18, 19*). More recently, Power and co-workers (*20*) reported that the addition of H₂ to Ge₂-alkyne analogs affords a mixture of Ge₂ and primary germane products. Metal-free systems that liberate H₂ are of interest for their potential in H₂ storage applications. Although much effort has focused on hydride salts (*21–23*), a recent report by Thorn and co-workers describes an organic "hydride" system that reacts with protic compounds to eliminate H₂, although the assistance of a metal-based catalyst is required (*24*). Despite these advances, no metal-free system is yet reported to effect both the clean liberation and addition of H₂.

Here we report a phosphonium-borate species that undergoes thermally induced loss of H₂ to generate the corresponding phosphine-borane. We discovered this reaction sequence in the course of our studies on phosphine-borane interactions. The well-known Lewis acidic polymerization cocatalyst $B(C_6F_5)_3$ behaves as a traditional Lewis acid with donor molecules to form simple Lewis acid-base adducts (*25, 26*). However, we have discovered that the sterically demanding secondary phosphine $(C_6H_2Me_3)_2PH$ reacts with $B(C_6F_5)_3$ to effect para-nucleophilic aromatic substitution, affording the zwitterionic phosphonium-borate $(C_6H_2Me_3)_2PH(C_6F_4)BF(C_6F_5)_2$ **1** (*27*) (Fig. 1).

The white, air- and moisture-stable solid **1** was isolated in 78% yield and exhibited a single phosphonium resonance in the $^{31}P\{^1H\}$ nuclear magnetic resonance (NMR) spectrum at –37.7 ppm as well as resonances in the ^{19}F NMR spectrum consistent with the presence of a BF bond and C₆F₄ and C₆F₅ rings. The corresponding ^{11}B NMR resonance revealed B-F coupling, and the ^1H NMR spectrum showed a doublet at 8.52 ppm from the PH fragment. Upon cooling to –15°C, the ^{19}F NMR resonances of the C₆F₄ bridge at –134 and –129 ppm split into doublets, consistent with inhibited rotation about the P–C₆F₄ bond. The thermodynamic barrier to this rotation was determined by variable-temperature NMR spectroscopy to be

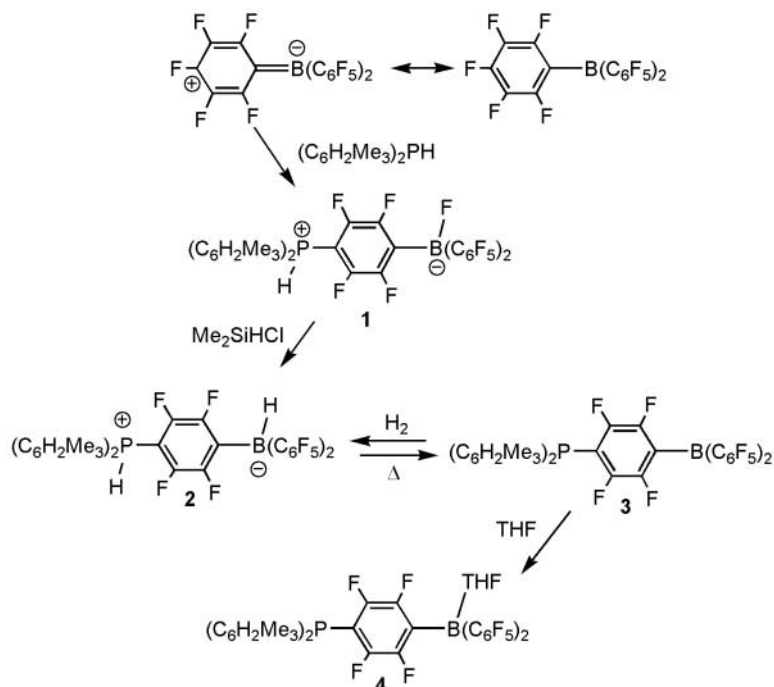Department of Chemistry and Biochemistry, University of Windsor, Windsor, Ontario N9B 3P4, Canada.

*To whom correspondence should be addressed. E-mail: stephan@uwindsor.ca

Fig. 1. Syntheses of compounds **1** to **4**.